Chapter 2

State-of-the-Art

In this chapter, a broad overview of the previous studies on drop and spray impingement, liquid film flow and three-dimensional, three-component velocimetry measurement techniques will be examined. A large amount of experimental, numerical and theoretical data from the literature will be summarized, in order to show the state-of-the-art in the fields at the moment and to point out which shortcomings are still present.

In general, impingement processes can be divided into two main categories: fundamental studies on single drop and/or monodispersed drop stream impingement onto dry or wetted surfaces, §(2.1); and studies focussing on spray impingement, §(2.2). In fluid mechanics, this division is based on the fact that theoretical models and numerical simulations for spray impingement are mostly based on models, derived from the results of single drop impingements, by using the superposition approach, since a full deterministic approach for spray impingement, where each droplet in the spray is considered individually, is impractical and would cost too much calculation time. However, relying on several studies, it is clearly shown that single drop impingement data cannot be used for describing spray impingement statistically. Sprays are a collection of a large number of drops, where the outcome of each individual drop impingement onto a liquid film is influenced by the unsteady wall film flow, as well as by the interactions with other impinging drops, both in the spray and during the interaction with the wall film, having a significant effect on the impingement processes. The theoretical and experimental investigations of this liquid wall film flow, formed by spray impingement, will be reviewed briefly, §(2.3). Finally, a short overview of the three-dimensional velocimetry measurement techniques will be examined, §(2.4), which can be used to measure the velocity fields inside the wall films during the spray impingement process.

2.1   Single drop impingement

The fluid mechanics behind a drop impinging on a dry or (partially) wetted surface has a great relevance in a large variety of technical, ecological, agricultural and meteorological fields. In most of the applications, the outcome of a drop impingement is described by a number of physical phenomena: droplet fluid flow itself, phase changes (interactions between the liquid (drop and wall film), the solid phase (wall) and the surrounding gas), heat transfer, liquid evaporation and solidification (in case of a heated wall and/or heated drops). From these physical phenomena, it can be deduced that the drop impingement is characterised by the physical properties of the drop liquid, the drop geometry and impinging velocity, by the texture and wetting properties of the target surface or the wall film properties on the target surface

for respectively a dry and (partially) wetted target, as well as by the gas boundary layer in the near-wall region in case of an applied shear flow.

2.1.1 Parameters influencing the impingement process

In order to understand the physics behind the drop impingement process, it is necessary to identify first of all the crucial parameters influencing this process. In the following, a detailed description of the individual physical properties will be given, whereafter they will be combined into different dimensionless numbers necessary for defining, comparing and modeling the different impingement processes.

Dimensional parameters

1. Drop liquid properties

    a Viscosity μ_d. The viscosity is responsible for the energy dissipation during the spreading stage of the drop on a dry surface or the expanding phase of the cavity inside the liquid wall film, appearing after impingement. To investigate the influence of viscosity, a modification of or a change to a different liquid is inevitable, unfortunately often combined with a change in density or surface tension of the fluid.

    b Surface tension σ_d. This parameter is a measure for the forces resisting the formation of an additional area. It has a very important role in the impingement outcome by defining the transition conditions, as well as in the post impingement status (spreading of the drop along a dry surface, shape of the corona, cavity collapse inside a liquid wall film, number of secondary droplets pinched-off from the crown after splashing, Stow and Stainer [162]).

    c Density ρ_d. The compressibility of the liquid is of high importance during the initial phase of impingement onto a dry wall. During this initial stage of impingement, the impingement pressure over the contact surface between target surface and impinging drop, being linearly proportional to the density of the drop, can rise considerably.

2. Drop geometry

    a Drop size D_d. Depending on the surface tension of the drop liquid, different drop sizes can be formed at the needle before drop pinch-off. The mass and the velocity of the drop after pinch-off determine the drop's kinetic energy. Stow and Hadfield [163] have shown that the impinging drop radius is directly proportional to the splashing threshold. They found that drops, having a radius smaller than 0.3 mm, were unlikely to splash at all on a dry surface, whereas drops with a radius larger than 0.8 mm would always splash. Furthermore, they noted that for drops having a larger diameter, the critical impingement velocity for splashing reduced.
    Stow and Stainer [162] found that an increase of the radius of the impinging drop resulted in an increase of the number of secondary droplets after splash. They subscribed this result to the creation of a thicker wall of the crown by a larger volume of the drop liquid.

b Drop shape. For most of the theoretical and numerical calculations the shape of the impinging drop is assumed to be spherical, although a falling drop will always be slightly deformed into an ellipsoid due to the aerodynamic forces acting on the drop when moving through the ambient air. Another cause for deviations from the spherical shape is the drop oscillation. In this case, the shape of the drop changes periodically from oblate to prolate before impingement, thereby changing the penetration depth of the vortex rings inside the liquid film after impingement, Rodriguez and Mesler [132]. These oscillations usually change the flow within the impinging drop. The effect of these oscillations on the impingement process is thought to be relatively small, as the amplitude of the oscillations gradually decreases in time due to the viscous dissipation, Lee and Lin [78]. Before impingement, when the drop is moving through the surrounding fluid, the friction between the surrounding fluid and the drop can also generate an internal flow, usually leading to a drag reduction, Hadamard [52] and Yasude *et al.* [197]. A quite common cause, also leading to a deviation from the spherical shape of the impinging drop, are the surfactants present in the drop liquid.

3. Drop incident velocity.

The drop impingement velocity is directly related to the deformation of the drop on impingement, as well as the radial flow of the drop liquid along the target surface or into the target liquid by impingement onto respectively a dry or wetted target. For normal impingement onto a liquid film or liquid pool, the cavity, appearing inside the target liquid after impingement, is growing in depth with a velocity approximately equal to $U_d/2$, U_d being the normal impingement velocity component. When the drop impinges onto a dry surface, the radial flow of drop liquid on impingement is driven by a force in the order of $\rho U_d^2/2$. Several investigations have shown, that the drop impingement velocity is proportional to the number of secondary droplets appearing, being more for higher impingement velocities. For the splashing regime, which will be explained in a later stage in detail, the drop impingement velocity influences directly the height and width of the corona, as well as the height of the liquid column that rises out of the center of the cavity (jet) after collapse of the cavity, i.e. the higher the impingement velocity, the wider and higher the corona and the higher the jet is.

4. Surrounding gas.

a Gas boundary layer. When a gas is flowing along the target surface, it will generate a boundary layer on it, hereby influencing the balance of the forces exerted on the impinging drop. Due to this boundary layer flow, the drop may deform and orient itself in the direction of the flowing gas. As a velocity gradient is present in the boundary layer, it will generate an additional lateral pressure difference around the moving drop, that leads to a lift force, the so-called *Saffman lift force*.

b Gas pressure. The influence of the pressure in the surrounding gas has not been investigated in detail. Engel [37] reduced in his experiments the pressure of the surrounding gas, in order to achieve higher drop impingement velocities. A light flash was observed during high speed impingement by Brunton [21]. This flash was assumed to be due to luminescence of the air trapped in between the impinging drop and the target.

5. Target surface characteristics.

    a Surface curvature R_c. The use of a curved target is two-folded: it makes the drop impingement more accessible for optical observations (Levin and Hobbs [83]) and the liquid flows off the point of impingement. For most applications, the ratio of the impinging drop diameter to the radius of curvature of the surface, D_d/R_c, is very small, meaning that the effect of the surface curvature on drop impingement can be neglected; hence, it is not an influencing parameter for the impingement process.

    b Surface roughness R_a. The surface roughness has a clear influence on the limiting conditions of the onset of splashing, as has been shown by several investigations. The splashing of a drop on a dry, rough surface has been investigated by Stow and Stainer [162] and Stow and Hadfield [163]. The first ones found that when they increased the roughness of the target surface, more secondary droplets were generated, which they put down to an increase of the amplitude of the perturbations in the target flow immediately upon impingement. Stow and Hadfield [163] measured the splashing limit of water drops onto a rough aluminium surface. They described their results by an empirical formula, $R_0 U_0^{1.69} = S_T(R_a)$, where S_T is the critical value for a drop to splash, depending on the surface roughness. This equation was confirmed by Range and Feuillebois [125] for water drops impinging on a rough aluminium plate, but they found different results for other liquids and other surface materials. They stated that in a more general way the splashing limit could be described by the empirical formula of Wu [194]. The effect of roughness on the splashing threshold is not only characterised by the surface roughness R_a, but also by the surface profile (random roughness, regular grooves, equidistant cavities).

    c Target surface. The surface on which the drop impinges, can either be a solid or a liquid. In case of a solid wall, the surface is usually defined by its roughness, whereas for a surface covered by a liquid film, the impingement process depends on the film thickness, as given in Table 2.1. For an increase in surface film thickness, the splashing limit is being influenced, as well as the number of secondary droplets and its size distribution. Tropea and Marengo [170] have shown, that for the impingement of an isopropanol drop, a small variation in film thickness, in the range of $0 < \delta/D_d < 0.25$, influences already the crown morphology, the secondary droplet sizes and the time scale of the splashing process.

Table 2.1: Impingement regimes for impingement on a wetted surface ($\delta = D_d/h$, $L_{nd} = L_a/D_d$, where h film thickness and L_a is the length scale of the roughness), Tropea and Marengo [170]

Regime	Defining range	Characteristics
Thin film	$L_{nd} < \delta/D_d < 3R_{nd}^{0.16}$	impingement depends on surface roughness
Liquid film	$3R_{nd}^{0.16} < \delta/D_d < 1.5$	dependence becomes weak
Shallow pool	$1.5 < \delta/D_d < 4.0$	impingement depends on film thickness
Deep pool	$\delta/D_d >> 4.0$	impingement independent of film thickness

    d Wall temperature, T_w. When the impinged surface is heated, a temperature difference between the surface and the surrounding gas or fluid is established, resulting in heat transfer and energy exchange from the surface to the surroundings. This transfer of heat leads to a change in the impingement dynamics, for example condensation or evaporation of the impinging drop.

Non-dimensional parameters

The influencing dimensional parameters, described above, are usually combined into non-dimensional numbers using the Buckingham Pi-Theorem, in order to get a better understanding of the relative influence of the above mentioned individual dimensional parameters on the impingement processes. In this paragraph, only the most common non-dimensional parameters are being described.

1. Weber Number

$$We_d = \frac{\rho_d U_d^2 D_d}{\sigma_d}$$

The Weber number is a measure for the relation between the kinetic energy of the droplet and its surface energy. A very large Weber number means that the influence of the surface tension forces can be neglected for the investigated drop impingement process. In case of a drop impingement, usually the normal component of the drop impingement velocity is taken for calculating the Weber number.

2. Reynolds number

$$Re_d = \frac{\rho_d |\mathbf{U}_d| D_d}{\mu_d}$$

This parameter gives the relation of the inertial forces of the drop to the dissipation acting on the drop.

3. Ohnesorge number

$$Oh_d = \frac{\mu_d}{\sqrt{\rho_d \sigma_d D_d}} = \sqrt{\frac{We_d}{Re_d^2}}$$

The Ohnesorge number represents the ratio of the dissipation to the surface tension of the impinging drop and is independent of the drop impingement velocity. Large Ohnesorge numbers indicate a greater influence of the drop liquid viscosity.

4. Relative film thickness
$$h^* = \frac{h}{D_d}$$

5. Relative surface roughness
$$R_a^* = \frac{R_a}{D_d}$$

In special drop impingement investigations, other parameters like the Froude number, $Fr_d = U_d^2/gD_d$, where the influence of the gravity on drop impingement is considered, and the Mach number, $Ma_d = U_d/c$, used in case of compressible drop impingements (Lesser [82], Dear and Field [28]), are used. The Laplace number, $La_d = \rho_d \sigma_d D_d/\mu_d^2$, has the same meaning as the Ohnesorge number. They are linked together by an inverse relationship, $La_d = Oh_d^{-2}$. A measure of the importance of the body forces (gravitational effects) compared to the surface tension forces is given by the Bond number, $Bo_d = \rho_d g D_d/\sigma = We_d/Fr_d$. A low Bond number (typically less than one) indicates that the drop impingement process is dominated by surface tension. For describing the duration of the drop impingement processes, the drop impingement velocity U_d and the drop diameter D_d are commonly used to make the time scale dimensionless, $t^* = tU_d/D_d$.

2.1.2 Impingement regimes

The impingement of a drop can be divided into many different scenarios, depending on the circumstances under which the impingement takes place. The fate of a collision depends on the parameters mentioned in the last section, among those the surface characteristics. Here, a clear distinction can be made between a solid or a liquid surface, each of which can be cold or heated. Bai and Gosman [4] identify seven possible impingement regimes that an impinging drop may undergo under different conditions, of which the most relevant ones are: (1) stick/deposition, (2) spread, (3) rebound and (4) splash. Analytical and experimental results have been used to determine a suitable combination of the dimensionless parameters to characterise the regime transitions. The boundaries between these different regimes and their parametric dependencies upon impingement are of particular interest. Different combinations have been found, of which most are listed in Table 2.2.

Table 2.2: Transition criteria for the different impingement regimes on dry and wetted surfaces

Surface	Transition	Criterion	Authors
Dry	deposition $\rightarrow$ splash	$Oh^{-0.37}We = K = f(R_a^*)$	Stow & Hadfield [163]
	deposition $\rightarrow$ splash	$Oh^{-0.4}We = 658$	Mundo *et al.* [102]
	deposition $\rightarrow$ splash	$Oh^{-0.7}We = 7.9 \cdot 10^{10}$	Walzel [181]
	deposition $\rightarrow$ splash	$1500 + 650/R_a^{*0.42} = K$	Han *et al.* [55]
	deposition $\rightarrow$ splash	$Oh^{-0.391}We^{0.305} = 0.85$	Vander Wal *et al.* [176]
	deposition $\rightarrow$ splash	$649 + 3.76/R_a^{*0.63} = K$	Cossali *et al.* [24]
Wet	deposition $\rightarrow$ rebound	$We_n = 5$	Bai & Gosman [4]
			Stanton & Rutland [161]
	deposition $\rightarrow$ rebound	$We_n = 20$	Lee & Hanratty [77]
	deposition $\rightarrow$ rebound	$We_n = 30$	Wang & Watkins [183]
	rebound $\rightarrow$ spread	$We_n = 10$	Stanton & Rutland [161]
	spread $\rightarrow$ splash	$We_n Re^{0.5} > K$	Stanton & Rutland [161]
	spread $\rightarrow$ splash	$We_n = 80$	Wang & Watkins [183]
	deposition $\rightarrow$ splash	$Oh^{-0.4}We = 2250$	Walzel [181]
	deposition $\rightarrow$ splash	$Oh^{-0.4}We - 1.04 \cdot 10^4$	Yarin & Weiss [196]
	deposition $\rightarrow$ splash	$Oh^{-0.4}We = 2100 + 5880h^{*1.44}$	Cossali *et al.* [24]
	deposition $\rightarrow$ splash	$(1500 + 650/R_a^{*0.42}) \cdot$	
		$\cdot[1 + 0.1Re^{0.5}min(h^*, 0.5)]$	Han *et al.* [55]
	deposition $\rightarrow$ splash	$Oh^{-0.17}We^{0.585} = 63$	Vander Wal *et al.* [176]
	deposition $\rightarrow$ splash	$1304 + 5032h^* = K$	Kalantari & Tropea [69]
	deposition $\rightarrow$ splash	$2074 + 870h^{*0.23} = K$	Coghe *et al.* [23]

In the stick regime, the impinging drop adheres to the surface in a nearly spherical form. This occurs when the impingement energy of the drop is extremely low. The transition criterion for the stick regime is, for an impingement on a dry or wetted surface, $We_n < 5$, where We_n is the Weber number calculated by using the normal component of the drop impingement velocity. This criterion is based on the experimental results of single drop impingements by Stanton and Rutland [161], Rodriguez and Mesler [132] and Walzel [181].

The rebound regime is characterised by an impinging drop which bounces off the surface after impingement. This regime can be observed when the surface is covered by a thin film and the impingement energy of the drop is low. In this case a thin air film is trapped between the impinging drop and the liquid surface film, causing a low energy dissipation, therefore resulting in bouncing. Different transition criteria for the rebound regime can be found in literature (Table 2.2), of which the most common one is given by $5 < We_n < 10$, based on the investigations of Rodriguez and Mesler [132] and Stow and Hadfield [163]. For spray observations, Lee and

Hanratty [77] found a transition to rebound at $We_n = 20$, whereas Wang and Watkins [183] used $We_n < 30$ for the rebounding regime in their simulations. During the rebounding process the impinging drop conserves its mass and diameter, thereby changing its direction and velocity. Several persons have investigated this change in drop direction and velocity after rebound, Watkins and Wang [184], Jayarantne and Mason [65] and Matsumoto and Saito [91].

The spreading of an impinging drop occurs, when the impingement velocity is moderate. The impinging drop spreads out equally over a dry surface, forming a thin film on the surface, or merges with the already existing liquid film for a wetted surface. The transition criterion for spreading is $We_n > 10$ and $WeRe^{0.5} < K$, given by Stanton and Rutland [161], where K is defined as the critical value.

The final important regime is splashing and occurs at a relatively high drop impingement energy. For the impingement of a drop onto a wetted surface a cavity inside the liquid film is formed with a corona-like shape at the periphery, having a rim at its top. This rim can become instable, thereby breaking-up into liquid jets having finger-like shapes, which, in turn, can break-up into many secondary droplets. In this regime, many quantities need to be calculated in order to describe the process in detail. These quantities include the proportion of the incident drop mass deposited onto the surface, as well as the sizes, velocities and ejection angles of the secondary droplets, Yarin and Weiss [196] and Mundo et al. [102].

The transition criteria for the splashing regime are analysed by many different persons, of which the most common ones are listed in Table 2.2. Here, a clear distinction can be made between drop impingement onto a dry surface, where the surface roughness R_a^* plays a very important role, and onto a liquid surface, where the thickness of the surface film h^* is of importance.

For a dry surface, Stow and Hadfield [163] found a correlation for the splashing limit in terms of Oh and We in the form of $Oh^{-0.37}We = K$, where the threshold K was found to be dependent of the surface roughness R_a^*. Mundo et al. [102] investigated the splashing limit for impingements on a dry surface by using a stream of monodispersed water/ethanol drops with mean diameters between 60 μm and 150 μm. The limit found was $Oh^{-0.4}We = 658$ with no difference for the two values of roughness used ($R_a^* = 0.03$ and $R_a^* = 0.86$), as the values for R_a^* were in the range where the splashing limit is nearly constant. In Figure 2.1 the values of the splashing limit of the measurements of Stow and Hadfield [163], Mundo et al. [102] and Coghe et al. [23] are plotted versus the non-dimensional surface roughness. The fitted curve of Cossali et al. [24] $K = 649 + 3.76/R_a^{*0.63}$ is also given in this figure.

The figure shows clearly that the splashing limit is a function of the surface roughness for a dry surface. The limit K decreases as the surface roughness is increased reaching an asymptotic value of about 650 for large values of R_a^*, meaning that the differences in surface tension and viscosity become far less significant in determining the splashing threshold. The fact that K increases sharply for decreasing surface roughness means that, for very smooth surfaces, the energy required to produce a splash upon impingement must be very high. The reason for this sharp increase of K is that the outflowing fluid at the contact line between the impinging drop and the smooth surface cannot be redirected in a direction normal to the wall, Levin and Hobbs [83] and Stow and Hadfield [163]. Han et al. [55] later argued that the curve $K = 1500 + 650/R_a^{*0.42}$ fitted the data in a better way, as Cossali et al. [24] had used the drop radius of the data of Stow and Hadfield [163] as the drop diameter.

Walzel [181] investigated the splashing limit with different mixtures of water/glycerine. His results for the impingement on a dry surface led to the following correlation, $Oh^{-0.7}We = 7.9 \cdot 10^{10}$, which is in contrast to the results from the other authors mentioned above. This dif-
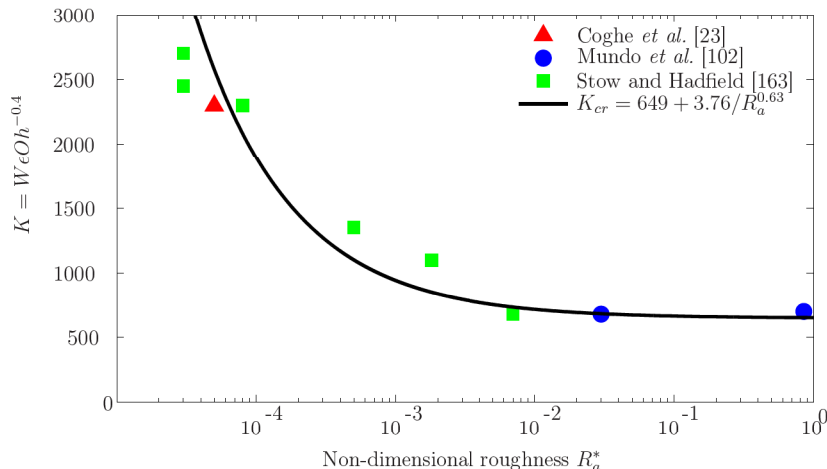
Figure 2.1: Splashing limit (K) vs. dimensionless surface roughness (R_a^*) for a drop impinging on a dry surface

ference is thought to be directly correlated with their very small non-dimensional surface roughness. The impingement of alkane and alcohol drops on a dry surface with a non-dimensional surface roughness of $R_a^* = 5 \cdot 10^{-3}$ was investigated by Vander Wal $et\ al.$ [176]. They found a relation for the splashing limit of $OhRe^{0.609} = 0.85$ in the range of $0 < Re < 7500$. By making the approximation that $Re^{0.609} \approx Re^{0.5}$ this relation was rewritten as $OhRe^{0.5} = Ca^{0.5} = 0.85$, giving a direct relation between surface tension and viscosity. They found that a high value for the surface tension acts to restrict splashing, whereas a large value for viscosity promotes splashing.

The presence of a thin film on the solid surface changes the splashing thresholds, as the splashing limit is a function of the film thickness in case of wetted surfaces. For a wetted surface, a splash criterion was proposed by Yarin and Weiss [196], who studied a train of drops impinging on an initially dry surface. They found that splashing occurred if the non-dimensional impingement velocity $U_{imp}^* = U_d(\sigma/\rho)^{-0.25}\nu^{0.125}f^{0.375}$ was greater than 18, where f is the drop frequency. For single drop impingements the ratio D_d/U_d is seen as the characteristic impingement time, which can be used to replace f, leading to the splashing criterion of Yarin and Weiss [196] of $Oh^{-0.4}We = 1.04 \cdot 10^4$.

Cossali $et\ al.$ [24] investigated the impingement of single drops of different water/glycerine mixtures on a thin liquid film in the range of $8 \cdot 10^{-2} < h^* < 1.2$ with a surface roughness of the solid wall of $R_a^* \cong 5 \cdot 10^{-5}$. The critical Weber numbers for splashing upon thin films are shown in Figure 2.2 for different values of the Ohnesorge number.

For each value of Oh the critical Weber number increases with an increase of the film thickness, meaning that a thicker film inhibits splashing due to the increased kinetic energy dissipation in the drop deformation process. A decrease of the Ohnesorge number decreases the splashing threshold, due to a decrease of the viscosity, responsible for damping the perturbations that are responsible for the jet formation and break-up. The correlation for the splashing limit for their measurements is given by $K = Oh^{-0.4}We = 2100 + 5880h^{*1.44}$, which holds for $0.1 < h^* < 1$ and $Oh > 7 \cdot 10^{-3}$. Han $et\ al.$ [55] used the data of Cossali $et\ al.$ [24] to improve the numerical model of O'Rourke and Amsden [111]. They proposed an alternative splashing criterion in which the effect of the film was reduced in the form $(1500+650/R_a^{*0.42})[1+ 0.1Re^{0.5}\min(h^*, 0.5)]$, valid for the case of shallow surface films $(h^* < 1)$ on relatively smooth
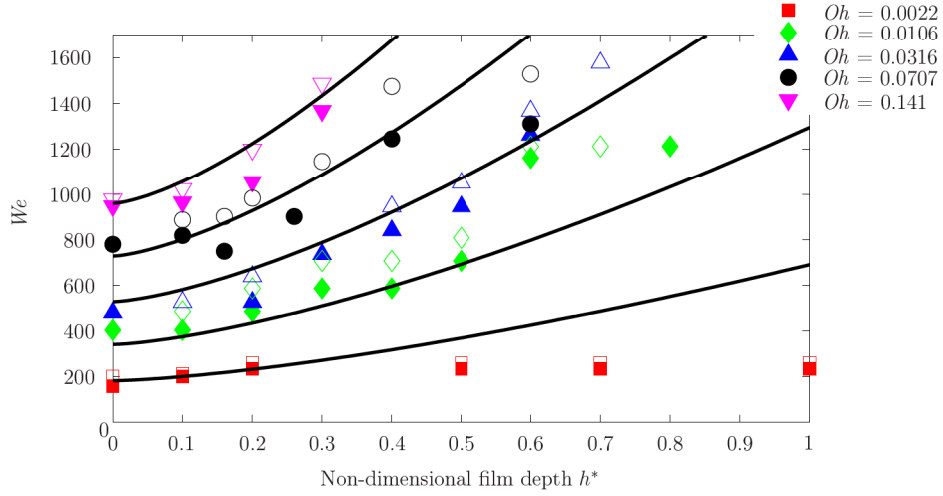
Figure 2.2: Critical Weber number vs. non-dimensional film depth for different values of Ohnesorge number (open symbols: observed splash; full symbols: observed deposit), Cossali *et al.* [24]. The curves define the correlation: $K = 2100 + 5880\delta^{1.44}$

surfaces.

Kalantari and Tropea [68] also found a relation for the splashing limit as a function of the surface film thickness by investigating the impingement of a spray onto films of different thicknesses. They identified four different liquid film regimes based on the critical Weber number for the onset of splashing. For thin films ($h^* = h/D_d \leq 0.1$) the value of the critical Weber number was found to be constant, whereafter it increased with an increase in h^* up to $h^* = 1$ and then decreased until approximately $h^* = 2$. For $h^* > 2$ it reached an asymptotic value corresponding to the impingement onto a deep liquid layer. For the range $0.1 \leq h^* \leq 1$ they found a splashing criterion of $K = 1304 + 5032h^*$. Coghe *et al.* [23] investigated the impingement of water drops onto a thin film ($h^* < 1$) and came up with a relation for the splashing limit of $K = 2074 + 870h^{*0.23}$.

Walzel [181] investigated the splashing limit with different mixtures of water/glycerine. The drops impinged on a glass surface covered by a thin film ($h^* = 0.1$) and a splashing threshold of $Oh^{-0.4}We = 2250$ was found, in good agreement with the measurements of Yarin & Weiss [196] and Cossali *et al.* [24]. Wang and Chen [182] showed that the splashing threshold was invariant with the film thickness at lower values ($0.05 < h^* < 0.1$) of the film thickness. Rioboo *et al.* [131] investigated the corona-splash and corona-deposition limits for impingements of single drops of silicon oils on thin liquid films in the order of $0.004 \leq h^* \leq 0.189$. They found that the limit between formation of the corona, hence splash, and deposition without formation of the corona is increasing in terms of the critical Weber number when the dimensionless film thickness decreases from 0.06 to 0.02, whereas at the same time the limit between formation of the corona and splash decreased. For $0.06 \leq h^* \leq 0.15$ the two limits, separating the deposition/corona formation and corona formation/splash regimes, were found to be constant at $K = Oh^{-0.4}We$ = 400 and $K = Oh^{-0.4}We = 2100$ respectively.

Vander Wal *et al.* [176] measured the impingement of alkane and alcohol drops on thin films of the same liquid and compared the results with their measurements of impingements of the same liquids on a dry surface. They found that the presence of a thin film caused a drastic shift in the splashing threshold for all the investigated fluids. In Figure 2.3, the Reynolds numbers are plotted versus the Ohnesorge numbers for the impingements on the thin film, as

well as the fitted curves $OhRe^{1.17} = 63$ and $OhRe = 20$, where the latter curve was obtained by approximating $Re^{1.17}$ by Re.
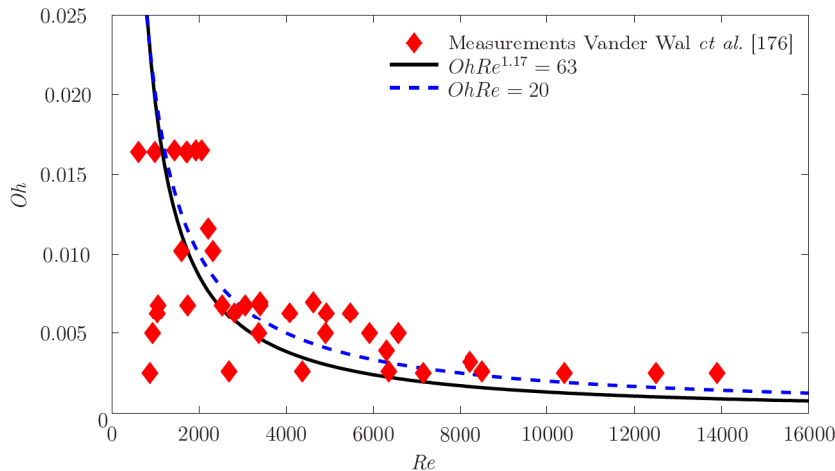

Figure 2.3: Splash behaviour on a thin film ($h^* = 5 \cdot 10^{-3}$): Re vs. Oh for different alkanes and alcohols (Vander Wal et al. [176])

They observed that for a drop impinging on a thin fluid film, splashing was seen to occur at far lower Weber numbers than for a dry surface. This difference could be explained by the kinematic discontinuity model of Yarin and Weiss [196]. Initially, the fluid within the liquid film is stationary, resulting in a very large velocity discontinuity between the liquid of the impinging drop, directed outward, and the initially stationary liquid of the film. This difference in velocity is larger than the velocity differences within the impinging drop that arise during the different stages of the drop impingement and drop deformation for an impingement on a dry surface. Therefore, the presence of the static film governs the splashing threshold while the fluid viscosity, absent in the approximation $OhRe = We^{0.5}$, plays only a secondary role in the splashing process.

2.1.3 Influence of several characteristic parameters on the drop impingement on a liquid film

Drop impingements on solid and liquid surfaces are a key element in a wide range of practical applications. The literature on this subject is therefore extremely rich. The focus here is on the single drop impingement on a pre-existing liquid film in atmospheric conditions. Much research has been conducted on the different aspects of the outcome of drop impingement in relation to the non-dimensional parameters mentioned above. This research can in general be divided into two main areas, i.e. the investigation of the impingement outcomes above the liquid surface and the ones below the liquid surface, where a cavity is being formed after impingement. The first area has been investigated thoroughly, where the main focus was directed on the maximum height and radius of the corona after splashing (Sivakumar and Tropea [156], Rieber and Frohn [129], Cossali et al. [25]), the maximum height of the jet after collapse of the cavity (Shin and McMahon, [153], Hobbs and Osheroff [60], Macklin and Hobbs [89]), secondary droplet sizes and velocities (Stanton and Rutland [161], Roisman and Tropea [139]) and the number and velocities of the droplets pinching-off the jet (Shin and McMahon, [153]). The investigation

of the outcomes below the liquid surface following drop impingement focussed mainly on the cavity shape (diameter and depth) in time (Engel [37], Morton *et al.* [100]), bubble entrapment regimes (Zhang and Thoroddsen [200], Oğuz and Prosperetti [106]) and on the vortex ring formation (Thoroddsen *et al.* [165]). In the following section, a small overview is given on those papers which address the aspects of the influence of the drop impingement Weber number, the surface film thickness, the shape of the cone of the cavity just before retraction of the cavity and the drop impingement angle on the outcome of the impingement process on a liquid film.

Influence of Weber number on cavity development

At low impingement velocities (low We and Fr) a drop impinging onto a liquid may coalesce, float or bounce. Cresswell and Morton [27] showed that during the first stages of impingement, capillary waves are seen to propagate up the impinging drop faster than the drop merges with the target liquid. At the same time a smooth, axisymmetrical capillary wave front propagates radially outwards from the impingement site. Liow [87] found that for very low Weber numbers the cavity survives for a short time only. When slowly increasing the Weber number, he noticed that the cavity shapes are not smooth, but initially oblate in shape and a sharp corner is formed on its side. While the capillary wave is traveling downwards along the surface, the cavity evolves into a more rounded shape. The growth of the cavity center slows down and the corner approaches the same depth as the base of the cavity; the base flattens out and the capillary wave converges to the cavity centreline. The capillary wave profiles become increasingly rounded with time and the base of the cavity center is forced downwards. Surface tension acts against this deformation and forces the cavity base to rise up and stop the inwards growth of the capillary wave. Rein [127] showed that the rapid initial cavity collapse evokes a rapid change in curvature at the cavity base, resulting in a vortex ring detachment.

When the Weber and Froude numbers are increased further, the bubble entrainment regime is entered. Over a limited range of drop diameters and impingement velocities, a small air bubble may be trapped beneath the collapsing cavity. Rein noticed that the entrapment of bubbles did not always accompany the formation of a thin high-speed jet, and concluded that small disturbances may suppress the entrainment. Pumphrey and Elmore [121] stated that "whether a bubble is entrapped is determined by a balance between the times at which the outward motion of the cavity walls is reversed at different positions". They showed that the bubble entrainment had a lower and an upper limit. Oğuz and Prosperetti [106] formulated that "if the downward motion of the liquid during the initial impingement phase is reversed before the cavity has grown to its maximum depth, the precise timing necessary for the entrainment of the bubble will be disrupted and the cavity will fill from the bottom with an upward-directed wave crest instead". They set the lower and upper regimes for bubble entrainment by the relation $We = A \cdot Fr^\alpha$, where $A = 41.3$ and $\alpha = 0.179$ for the lower boundary and $A = 48.3$ and $\alpha = 0.274$ for the upper bubble entrainment boundary. A characteristic nipple was found at the base of the cavity for the lower bubble entrainment regime, responsible for the formation of the bubble. Liow [87] stated that the upper limit is set by the capillary waves on the cavity wall. When these waves meet to form a sharp non-axisymmetric point at the cavity base, no bubble will be entrained.

Several studies (like Liow [87], Morton and *et al.* [100], Pumphrey and Elmore [121] and Prosperetti and Oğuz [120]) have been conducted to investigate the bubble pinch-off regime. The entrainment regime is defined by different cavity dynamics than for the coalescence regime

and no vortex rings are found. The deeper cavity associated with increased impingement energy has a cylindrical shape with a rounded nose. As the downward moving capillary wave continues to approach the base of the cavity, the cavity stops growing and reverses its direction at different times at different positions. The capillary wave is being focussed into the cavity base, and while the tip of the cavity keeps growing, the sidewalls reverse their outward motion and start moving inwards with a velocity that increases with depth. During collapse, the capillary wave meets at a point just above the cavity base, which leads to the formation of an air bubble that detaches from the bottom of the cavity. For higher Weber numbers, the cavity takes longer to begin collapsing, allowing the sharp corner to form sharper edges. This leads to the cavity taking a polygonal shape, which reduces to an inverted triangle just before bubble entrainment. After pinch-off, the sharp point retracts and when the retraction is rapid enough, a high-speed Worthington jet is formed. With increasing drop impingement speeds, the point is sharper and the jet faster. Pumphrey and Elmore named this the "regular entrainment regime", since for a small range of drop velocities and diameters they observed that the cavity collapse always led to bubble pinch-off. Longuet-Higgins [88] investigated the half cone angle of the sharp point appearing just before bubble pinch-off. He found that by assuming a self-similar potential flow and neglecting gravity and surface tension, there exists a limit cone angle of the sharp point of 109.5° past which the pressure gradient is unable to further increase the aperture of the cone.

With further increase of the impingement velocity, the bubble entrainment and thin jet regime are left behind and the regime of the appearance of broad jets - similar to those first photographed by Worthington - after the cavity collapse is entered. In this regime, usually one or two drops are pinched-off the central jet with a low velocity and the sides of the cavity form a crown which breaks up to form small splash droplets. These jets have a similar diameter as that of the initial drop and rise to a maximum that increases with increasing drop impingement velocity. Engel [37] investigated the impingement of a drop close to terminal velocity onto a deep pool and found that a thin cylindrical film, formed as a crown at the mouth of the impingement cavity, rises high enough that it loses its momentum and closes over the cavity due to surface tension to form a large bubble. At the moment that this cylindrical film closes, a weak upward jet and a strong downward moving jet are formed of which the latter one merges with the upward jet formed during the collapse of the cavity.

Influence of film depth and viscosity on cavity development

Shin and Mcmahon [153] investigated the height reached by the highest-flying ejected droplet for a drop impinging onto a pool of variable depth ($h^\star = h/D_d = 1.2$, 2.0 and 2.9), or as they called it, "the tuning of a splash". They found that the height reached is greatest when the depth of the target liquid is equal to the radius of the hemispherical cavity formed by the impingement. They saw that a wavy instability is formed at the air-liquid surface of the cavity as it is growing, apparent at all depths. It grows more rapidly when the cavity starts to collapse. The growth and the collapse of the cavity is well synchronised (at and above the tuning depth), until the largest cavity diameter is reached. From this instant, the cavity at tuning depth lags behind the deep-water cavity.

The influence of the pool depth on the change of the cavity and the Rayleigh jet have also been measured by Macklin and Hobbs [89]. For values of $h^\star$ between 8.7 and 4.3 (deep pools) they found that the manner and rate of the formation of the cavity do not differ much. They saw that the cavity expands as a hemisphere to a maximum value of $2.6D_d$. They also

measured the velocity of the cavity expansion and found that this cavity penetration decreases in an exponential manner with time from 1.1 m/s to 0.5 m/s. By decreasing the pool depth up to $h^\star = 3.9$ to 2.6, they marked a slight flattening of the base of the cavity. They stated that this flattening results in drastic changes of the pressure gradients in the liquid during the formation and collapse of the cavity, as the pressure gradients become vertical. For $h^\star < 2.6$, the pressure gradients in the liquid are more horizontal due to the closeness of the wall, preventing liquid flowing into the cavity from below.

Shin and McMahon [153] and Fedrochenko and Wang [42] investigated the change of the cavity for shallow pools and the influence of the viscosity on the cavity. Shin and McMahon stated that the radius of the cavity does not change with the depth of liquid up to the tuning depth ($h^\star = 2.0$). When the radius of the cavity matches the liquid depth, the stem at the bottom of the cavity is delayed in retracting upward by the condition that no fluid velocity is allowed in a direction normal to the floor of the pool. The curvature of the cavity bottom is larger when a stem is present, as the capillary wave along the wall distorts the cavity shape, resulting in a larger cone angle at the bottom of the cavity. This larger cone results in larger surface tension forces responsible for a higher pressure difference across the air-liquid interface during jet formation than would be the case in a deep pool. The cavity remains deep, until a very late stage of its collapse, meaning that hydrostatic forces aiding the formation of the Worthingtom jet are greater in shallow pools than in deep pools. As a consequence of the delayed upward retraction of the bottom of the cavity, the jet is not only narrower, but also faster.

Fedrochenko and Wang [42] investigated the influence of the viscosity on the cavity, by comparing the impingement of a drop of water onto a shallow water pool and a water/glycerol drop onto a shallow water/glycerol pool of $h^\star = 2$. They found that for the impingement of a water drop onto a shallow water pool the cavity touches the bottom and the shape of the cavity is distorted by capillary waves, whereas in the other case (water/glycerol having a higher viscosity) the cavity almost touches the bottom and the shape of the cavity is smooth.

Influence of drop impingement angle

Compared with normal drop impingement, the investigations of an oblique impingement of single drops is much scarce. Zhbankova and Kolpakov [201] studied the influence of the impingement angle on the collision outcome with a liquid film. They observed coalescence and bouncing of the imping drop and investigated the influence of the imping drop's Weber number and the imping angle on the coalescence probability. As the Weber number in their experiments was very low ($We_n < 3.2$), they did not observe splashing. Schotland [147] and Jayaratne and Mason [65] measured the impingement of water drops onto water surfaces, thereby determining the regimes for bouncing and coalescence. They performed their experiments in the low Weber number range ($0.1 \leq We \leq 4$) for different impingement angles α ($10 \leq \alpha \leq 90°$). All authors found a threshold Weber number between rebounding and coalescence, dependent of the imping angle, with $0.8 \leq We_{cr}(\alpha) \leq 3$.

Leneweit *et al.* [81] studied the oblique impingement of single glycerine/water drops on deep pools at various angles of incidence and for a wide range of impingement Weber numbers ($15 \leq We \leq 249$), where α was varied between 5° and 64°. They observed that in the whole range of Weber numbers investigated, when the impingement angle α is smaller than 14°, some drops rebound after initial coalescence and depression of the imping surface, with the rebounding drop diameter of about the same size as the imping drop diameter. Most impinging drops,

however, coalesce permanently without rebounding. For $We < 140$ and $\alpha < 23°$, they observed that the impinging drops spread out evenly on the impinging liquid with no visible immersion. For $\alpha > 23°$, a partial immersion of the drop fluid was found, either in the rear part of the cavity, or behind the front of the spreading drop. The partial immersion in the rear part of the cavity was found for all impingements with $\alpha > 23°$, whereas immersion behind the front of the spreading drop occurred within two ranges: for $We_n > 10$ and $We > 50$ and for $We > 140$ and $\alpha < 23°$.

The oblique impingement of single water drops onto a plane water surface in the Weber number range of $(7 \leq We \leq 818)$ at various angles of incidence $(11° \leq \alpha \leq 75°)$ and surface film thicknesses was investigated by Okawa et $al.$ [107]. By investigating the critical value for the splashing limit, they observed that this value K decreased with an increase of the angle of incidence, when the normal component of the impinging drop velocity was used for calculating K. This in contrast to the roughly constant value of $K \approx 2100$ when the absolute drop velocity was taken. For angles of incidence larger than $50°$, the value of K increased again. The effect of the liquid surface film thickness h^* on the splashing limit was investigated for impinging angles between $10° \leq \alpha \leq 50°$. Here, no clear dependence on h^* was found, in comparison to the measurements of Cossali et $al.$ [24] for viscous liquids and those of Rioboo et $al.$ [131] for very thin liquid films, where a clear influence of h^* on K was found. Okawa et $al.$ [107] explained this difference by the fact that they only used water for their experiments and measured the impingement for rather high film thicknesses.

Investigation of the cone just before bubble pinch-off and retraction

The pinch-off of a liquid drop is an example of a hydrodynamic singularity and has become paradigmatic for self-similar behaviour in fluid dynamics: after appropriate rescaling, the shapes of the pinching neck at different times can be superimposed onto a single shape, independent of the initial conditions. Bubble collapse appears to be a special case of an inviscid fluid drop breaking up inside another inviscid fluid; the minimum drop radius scales like $(R_{neck} \propto \tau^{2/3})$, where R_{neck} is the radius of the neck expressed in the time τ remaining until collapse. If the dynamics near the singularity are solely governed by liquid inertia, then the radius of the neck scales as $h \propto \tau^{1/2}$. The collapse may be slowed down by viscosity $(h \propto \tau)$ or surface tension $(h \propto \tau^{2/3})$, or accelerated by the inertia of the gas flowing inside the neck, leading to $(h \propto \tau^{1/3})$.

Bergmann et al [11] investigated the inverse pinch-off of the collapse of a gas-filled neck surrounded by a liquid. They pulled a disk quickly through a water surface leading to a giant axisymmetrical void, which first expands until the hydrostatic pressure drives the walls inward. The inward moving walls collide and cause a pinch-off at some depth below the undisturbed free surface. The energy focusing of this violent collapse creates a strong pressure spike on the axis of symmetry, which releases itself and creates an upward and downward jet. They found that the pinch-off of an air bubble in water is not self-similar, even by the exclusion of effects of air, viscosity and surface tension, but governed by power laws with non-universal, Froude-dependent components. Very near the pinch-off, the void profile approaches a cylindrical shape, a regime that is approached earlier as the Froude number is larger. Self-similarity exists only in the limit of $Fr \to \infty$, where the influence of gravity is negligible and the collapse is truly inertially driven.

The collapse of an axisymmetric cavity or bubble inside a fluid of small viscosity, like water, was investigated by Eggers et al [31]. They neglected any effects of the gas inside the cavity as well as of the fluid viscosity. The air-water system corresponds to an inner fluid of vanishing

inertia, surrounded by an ideal fluid. They found that the minimum radius of the cavity scales like ($h \propto \tau^{\alpha}$), where $\alpha = 0.5 + 1/(4\sqrt{-ln\tau})$. They stated that the breakup is much faster than in the fluid-fluid case, and that the surface tension must become irrelevant as a driving force. Furthermore, as α is a function of τ, it depends on the initial condition.

Dripping is usually associated with fluid motion, but Ishiguro et al [62] have investigated the analogous phenomenon of a ^{3}He crystal growing and melting under influence of surface tension and gravity. They described the pinch-off by a purely geometric equation of motion, and neglected viscous dissipation and inertia forces. For most of the neck's evolution, a scaling exponent of the power law close to $h \propto \tau^{1/3}$ was found, as a result of the slowly decaying transients of the pinch solution. The shape of the neck is symmetric with respect to a horizontal plane, contrary to what is observed for ordinary fluids. The minimum neck radius goes to zero like a power law, scaling as $h \propto \tau^{1/2}$, in analogy to fluid pinch-off. They did not find a universal law governing the recoil of the crystal tips after pinch-off, but for very early times there is an asymptotic regime of scale factor 1/2.

They also analysed the retraction of the two tips of the crystal after it pinched-off, and found that the half gap between the two tips follows the curve $D \propto t^{1/3}$, where t is the time after pinch-off. This situation is very different from the fluid breakup, where a universal solution for the retraction is found, due to the different character of the similarity variable before impingement, as the receding tip is invading a region where the solution depends on the initial conditions. They modeled the shape of each drop just after detachment as a cone with half angle θ which terminates as a spherical tip with radius R and found, for simple geometries, for the non-dimensional half gap the relation $d = D/R_0 = R(1 - sin\theta)/sin\theta$ and for the time dependence $d^2 = 4(1 - sin\theta)^2\tau/sin^2\theta$.

2.2 Multiple drop impingement

Spray impingement, involving multiple drop interactions, is being experienced more complicated than the process of single drop impingement. This is because for spray impingement many interactions take place at the same time, i.e. impinging drops may interact with neighbouring drops, as well as a two-sided interaction between impinging drops and the post-impingement products, like the corona and pinched-off secondary droplets. Exactly these interactions make the investigation of spray impingement on a solid or liquid surface very interesting, but a clarification of the process extremely difficult. The experimental and numerical research involving spray impingement has focussed mainly on the heat transfer between the heated surface and the impinging spray forming a thin liquid film on this surface, as well as the identification of the different processes happening and products appearing during and after the spray wall interaction (secondary droplet diameters and velocities).

Most of the present models for spray impingement are based on the assumption that the results obtained for single drop impingement can be extrapolated to the case of a spray by using the superposition algorithm, where the same model for a single drop event is applied to each drop of the spray. During the impingement of a spray, multiple drops are successively and/or simultaneously impinging onto the substrate. These multiple drop impingements result in complicated interactions of drops before impingement, with possible resulting satellite drops, as well as of the coronas formed after impingement, which can lead in corona interaction and destruction and, depending on the inter-drop spacing and phase, in larger reatomised droplets. These interactions are mostly not taken into account when applying models based on the superposition principle. For very sparse sprays, where the drop density is low and interactions

between impinging drops and coronas will not take place very frequently, the superposition principle is presumably valid, but for most practical spray impingement applications this is not a very good approximation. Several studies (Roisman *et al.* [133], Tropea and Roisman [171], Roisman and Tropea [134], Han *et al.* [55]) have shown that this assumption is not reliable in case of dense sprays - like diesel sprays - by showing that the secondary droplet sizes and the deposited mass rate were considerably underpredicted by applying superposition. Several investigations have been made for correctly taking into account the effects of interactions due to spray impingement.

In order to investigate the influence of the multiple drop impingement on the interactions and impingement outcomes, several authors have studied the successive and/or simultaneous impingement of two or more drops. Richter *et al.* [128] varied the impingement frequency of a monodispersed drop stream to investigate the interaction between successive impingements. The results showed that this led to significantly larger secondary droplets moving more or less parallel to the impingement surface. Barnes *et al.* [8] studied the phenomenon occurring when two streams of identical monodisperse water drops impinged symmetrically on either side of the apex of a sphere. The distance between the two streams was kept sufficiently close in order to assure interaction and collision between the two resulting coronas to occur. A "*hump*" of liquid was observed to be produced between the two coronas, the height of which changed by changing the inter-drop phase and spacing, and reatomized droplets were seen to pinch-off, being larger and slower than for a single drop impingement. Tropea and Roisman [171] suggested a model to account for this interaction, which led to a better prediction of the impingement outcome. Later, Sivakumar and Tropea [156] and Cossali *et al.* [25] showed that not only the successive drop collisions and crown interaction change the characteristics of the secondary droplet formation, but also the local variations of the liquid film, induced by drop impingement, resulted in a change of the crown development and therefore the secondary atomization. Roisman and Tropea [135] and [139] observed that multiple drop impingements result in significant pressure fluctuations inside the liquid surface film.

Spray impingement onto a dry surface or a wetted wall has been thoroughly investigated in the last centuries, by means of different experimental techniques such as laser-Doppler velocimetry and phase-Doppler velocimetry, light extinction methods, high speed camera visualisation, shadowgraphy and tomography, simulation with gas sprays and hot wire anemometry. Of all these investigations, a small overview will be given below. At the beginning the studies were mainly focussed on the macroscopic characteristics of the spray, like the spray images, spray tip penetration, temporal development of the height and radius of the spray after impingement, etc. (Watkins and Wang [184], Wang and Watkins [183], Park and Lee [114], Ko and Arai [71] and [72], Katsura *et al.* [70], Ebara *et al.* [30]). Regarding the aspect of the spray contour, several studies have shown the existence of a narrow zone in the wall spray area close to the impingement point. As time prolongs, the spray spreads along the surface, leading to an increase of the wall spray thickness in the frontal region (Fujimoto *et al.* [45]), correlated with the existence of a wall-bounded vortex in the peripheral region of the wall spray. In this region, most of the air entrainment occurs, leading to an increase of the spray thickness (Katsura *et al.* [70]). The existence of this vortex has been proven by several authors by means of phase-Doppler anemometry and tomographic techniques.

A fuel spray, particularly a Diesel injection spray, consists of relatively small ($\approx$ 5 - 20 μm) droplets moving with a relatively high ($\approx$ 50 - 300 m/s) velocity. The spray is so dense that the theoretical or experimental investigation of the structure of the spray, the details of atom-

ization, propagation and impingement, is an extremely difficult task. In the experimental work of Katsura *et al.* [70], Fujimoto *et al.* [45], Tomonaga *et al.* [167], Ebara *et al.* [30], Mohammadi *et al.* [98] the fuel (or oil, having the physical properties similar to those of fuels) spray was injected into a chamber. The spray was not steady, its duration being of the order of one to several milliseconds. The shape of the impinging spray, normal and inclined, was observed and several parameters were measured, like the length of the spray path along the wall, L_{path}, its thickness above the wall, h_w, as well as the shape of the spray before and after impingement. The data were usually reported as a function of time after the start of injection. Among the varied parameters were the impingement angle, distance from the wall to the nozzle, ambient and injection pressure. Desantes *et al.* [29] investigated the high pressure Diesel spray impingement in a high density gas against a flat surface, by changing the impingement angle and the gas density. They observed that when the impingement angle was decreased, the wall spray penetration in the principal direction increased, whereas for a fixed impingement angle, the spray penetration decreased for increasing gas density.

To compare the behaviour of an impinging spray with that of a free spray, Ebara *et al.* [30] introduced the *spray path penetration*, which was determined as a function of the radial and axial penetrations of the impinged spray. The definition of this spray path penetration is shown in Figure 2.4.
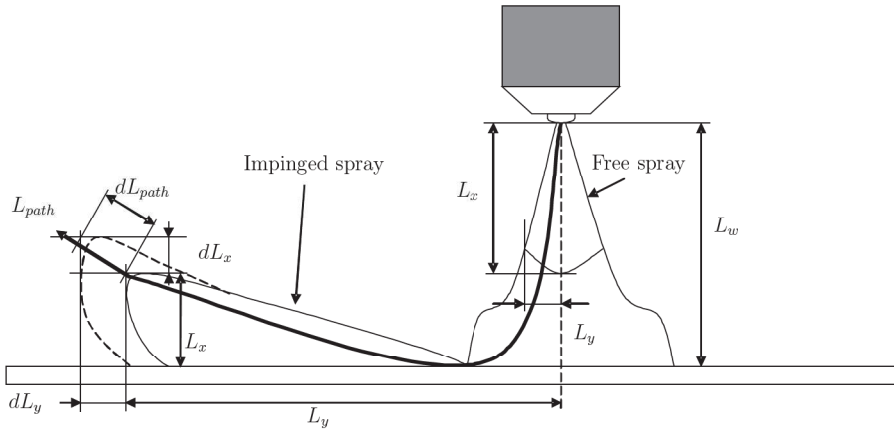
Figure 2.4: Definition of spray path penetration (Ko and Arai [71])

By integration of an imaginary spray tip movement, which was composed by a lateral and axial penetration of the spray, the path of an imaginary spray tip was considered. The length of the path that the spray tip traveled after the injection of the spray was calculated from two spray tip images taken a time distance dt apart. The L_{path} could be calculated from the following equations:

$$dL_{path} = \sqrt{(dL_x)^2 + (dL_y)^2} \tag{2.1}$$

$$L_{path} = \int_0^t \sqrt{\left(\frac{dL_x}{dt}\right)^2 + \left(\frac{dL_y}{dt}\right)^2}\, dt \tag{2.2}$$

The scalar length along the spray movement before and after impingement could be presented by this spray path. Ebara *et al.* [30] suggested an empirical equation of the spray path, given by:

25

$$L_{path} = B_i \sqrt{T_{ASOI} - T_w} + L_w \tag{2.3}$$

where B_i was formulated as

$$B_i = (56.1 - 0.36 L_w - 0.39\theta + 0.0033 L_w \theta) \cdot \left(\frac{1.5}{P_{amb}}\right)^{0.25} \tag{2.4}$$

$$\theta = 90 - \theta_w \tag{2.5}$$

In the above equations, T_{ASOI} is the time after start of injection, T_w is the impingement time and θ_w is the wall inclination angle, in case of impingement on an inclined surface.

Besides the many studies on the macroscopic characteristics of the spray and spray impingement, the information on the Sauter mean diameter (SMD) distribution of the investigated spray and the velocity distribution of the primary and secondary drops is also very useful for spray modelling. Özdemir [112] studied the outcome of the oblique impingement ($\alpha = 20°$) of an unsteady two-phase jet on heated surfaces. He came to the conclusion that a new size class with larger droplets was generated after impingement, due to the added mass of the film liquid to the penetrating drops. Furthermore, the resulting larger droplets tended to stay close to the wall within the impingement region with small vertical velocities. Schünemann et al. [148] investigated the influence of the governing parameters, like injection pressure and wall temperature, on the characteristics of the impinged spray. They measured the SMD of the impinged spray at three different points positioned 2 mm above the wall and found that with increased injection pressure the secondary droplet diameters showed a decrease in diameter due to better primary atomization.

The atomization characteristics of a fuel spray impinging on a wall were also investigated by Park and Lee [114], who measured the influence of the injection and ambient pressures, the wall temperature, the inclination angle of the wall and the distance between the injector and the wall. They stated that, in comparison with a free spray without impingement, the atomization performances of the impinged spray were better, because of the secondary atomization caused by the impingement on the wall. For small distances above the wall, the radial velocity of the droplets increased in the region near the mean axis and decreased in the outer regions. When this distance was increased, the effect of the impingement was negligible. By changing the wall inclination, it was found that the SMD of the secondary droplets was smaller for the case of perpendicular impingement, and increased for increasing angle of incidence, due to the lower secondary atomization by the presence of the wall.

The impingement of coarse sprays on vertical walls with and without a liquid film was investigated by Weiss [186], where the primary and secondary spray were characterised as a function of the injection pressure and the impingement angle. The influence of the injection pressure was found to have only a slight effect on the secondary droplet sizes, whereas a change in the impingement angle resulted in a considerably smaller spread of the droplet sizes, due to splashing and interaction effects. When the distance between the nozzle and the wall was increased, a fine fraction of the secondary spray was reduced, as a large amount of the very fine droplets were present only in the near-wall region. Concerning the droplet velocity components tangential and normal to the wall, the results showed that the latter was relatively constant for all investigated impingement angles and injection pressures, whereas the tangential velocity component increased with increasing injection pressure, but decreased for steeper impingement angles due to a lower tangential momentum provided by the primary spray. As a result of the dominating effect of the interactions of the primary drops with the secondary droplets for

steeper impingement angles, the influence of the injection pressure was reduced. Desantes *et al.* [29] measured the evolution of the SMD and mean velocity as a function of time at three measurement points 3 mm downstream of the impingement point at distances of 0.5, 1.5 and 3 mm above the surface and for three different gas densities. They observed that for high gas densities, the Sauter Mean Diameter increased when the measurement points lay far away from the spray tip. They explained this observation by the local increase of fuel concentration that is caused by the presence of the wall resulting in drop coalescence.

Concerning the modelling of spray impingement onto a solid substrate, there are three main approaches.

The first approach describes the process as a simple superposition of single drop impingement events. Models of varying degrees of complexity are thus formulated on the basis of available data for the single drop impingement, in some cases with a complete neglect of the actual fluid mechanics or with a disregard for some influencing parameters. Examples of this approach can be found in the models for the fuel spray impingement in Bai and Gosman [4], Stanton and Rutland [161], Han *et al.* [55], Bai *et al.* [6]. For water sprays, several authors have designed models incorporating the thresholds for rebound, spreading and splashing of impinging drops, for dry and wetted, as well as for rough and smooth surfaces (Samenfink [144], Mundo *et al.* [103]). A similar approach was used in the model Lee and Bergman [76] for thermal plasma spraying, accounting for the solidification of the droplets. Such models are based on the experimental (Harlow and Shannon [56], Cossali *et al.* [24], Rioboo *et al.* [130]) or theoretical (Yarin and Weiss [196]) studies of the single impingement of a liquid drop onto a steady uniform liquid film or onto a deep pool (Oğuz and Prosperetti [106]).

As has been mentioned already at the beginning of this section, several investigations (Roisman *et al.* [133], Tropea and Roisman [171], Roisman and Tropea [134], Han *et al.* [55]) have shown that the superposition principle does not give satisfactory results between the measurements and the analytical models, because of the interactions of the impinging drops and the coronas on the surface. In order to account for these interactions during spray impingement, different models have been presented. In most of the numerical simulations, the model of O'Rourke [109] is used for describing the drop collision process. By using the classical kinetic theory based on the assumption that the drops were uniformly distributed inside the sprays and the drop collisions had similarity to the molecular collision process, O'Rourke derived the equation of the collision probability. Using the equations for the conservation of mass, velocity and energy between the drops before and after impingement, he also modelled the post-impingement characteristics of the droplets. His model, however, does only take into account coalescence and grazing separation, but not reflective and stretching separations and the subsequent formation of satellite droplets. Ko *et al.* [73] investigated the interspray impingement system, where two solid cone sprays directly impinged, resulting in drop collisions with high relative velocities. They found that the model of O'Rourke substantially overpredicted the droplet sizes and failed to predict the overall spray shapes correctly.

Many different authors (Qian and Law [122], Estrade *et al.* [40], Brenn *et al.* [18]) have shown that satellite droplets are formed during the collision of drops and that the size of the droplets decreases after these collisions. Georjon and Reitz [49] proposed a model for drop-shattering collision. They assumed that when two drops collided with a sufficient high collision Weber number, they were transformed into a long cylindrical liquid ligament. Under the impulse of the collision this ligament elongated, and, based on the Rayleigh linear jet break-up theory, capillary wave-induced distributions grew and eventually led to break-up into droplets, when the time needed for the distributions to develop was shorter than the time taken by the two

ends of the cylinder to retract. They assumed, however, that the shattering regime did not depend on the impingement parameter, nor on the size ratio of the colliding drops. Furthermore, their model was based on the assumption that the satellite formation and shattering collision produced equal-sized droplets. In a Diesel spray, the collision phenomena are, however, much more complex.

Another numerical model considering drop collision-induced break-up with the formation of satellite droplets was proposed by Ko and Ryou [74], based on the conservation of drop mass, momentum and energy before and after the collision. For the collision of equally-sized water drops, by changing the impingement parameter from 0 (head-on collision) to 1 (grazing), they found that, in the stretching separation regime, the number of satellite droplets formed after collision is the highest in the range from 0.4 to 0.6 for the impingement parameter. Below this regime, the number of satellite droplets increased with increasing impingement parameter, because of the increase in stretching energy, whereas above this regime, less satellite droplets were formed due to the decrease in interaction between the two colliding drops. For the reflexive separation regime, most satellite droplets were formed in the case of a head-on collision, as the stretching effects induced by off-centre collision reduced the reflexive separation.

The second approach frequently used in the description of spray painting (Ye et al. [198], Eres and Schwartz [39]) neglects completely the inertial effects associated with the spray impingement. The negative flux of secondary droplets and the momentum of the oscillations of the liquid in the film on the wall are also neglected. The spray is considered only as a source of the liquid volume flux. Next, the motion of the deposited liquid film is described using the governing equations of hydrodynamics of falling films.

The third approach is based on the direct numerical simulations of the spray impingement. Böhm *et al.* [15] and Böhm [14] used a commercially available numerical code, based on the volume-of-fluid method, to simulate not only a single drop impingement onto a dry wall, but also a multi-drop impingement (normal impingement of maximum 22 identical drops, uniformly distributed in space). This multi-drop impingement led to the creation of an oscillating film. Polydisperse spray impingements, however, are characterized by different length and time scales. The characteristic length scale of the film fluctuations may be much larger than the drop diameter and the characteristic time of such fluctuations is much larger than the typical time of drop impingement. This means that, in order to describe the spray impingement numerically, a relatively large domain size is required with a very fine mesh. Second, the time step must be small enough to describe each drop impingement event. Moreover, a relatively large time duration must be simulated, such that a large number of drops impinge, in order to represent the real statistics of the spray. This problem is too complex and expensive even for modern supercomputers.

2.3   Liquid wall film flow

At very early stages during spray impingement onto a wall the droplets of the spray impinge on a dry surface, leaving their deposited mass on the surface in the form of small discs. As time continues, more and more droplets are impinging, resulting in an accumulation of the deposited mass on the surface and a continuous liquid film is being formed. Due to inserted mass and momentum into the forming film by the impinging droplets, the liquid film becomes thicker and, at the same time, spreads outward along the surface. Due to the continuous impingement of droplets on this liquid film, its surface is subjected to strong disturbances, creating a moving and fluctuating liquid film. For relatively sparse sprays secondary droplets are produced by the splashing of the impinging droplets and their mutual interactions, whereas for dense

sprays, like Diesel sprays, it is this fluctuating surface film that creates the secondary droplets. The focus here is on these studies that investigate the film dynamics during spray impingement.

2.3.1 Experimental investigations of films formed by impinging sprays

Not much research has been done until now to investigate in detail the film dynamics during spray impingement onto a solid surface. Most of the studies found in literature have focussed on the spray shape on the surface after impingement, as well as on the fraction of liquid mass deposited onto this surface.

Saito et al. [143] developed a laser reflection method using a prism, and observed the evaporation of the fuel film. They found that the diameter of the fuel film decreased with increasing wall surface temperature. The relation between the behaviour of a spray impinging on a vertical surface and the fuel mass adhered on this surface was investigated experimentally by Ko and Arai [71] and [72]. They investigated the influence of the wall distance and of the ambient pressure on the spray shape, adhering fuel mass and film thickness and diameter right after spray injection into the pressure chamber. They found that the growth of the impinging spray along the wall was faster than that of the fuel film, hence, the spray after impingement increased separately from the wall. With increase of the nozzle-to-wall distance the fuel film diameter, as well as the fuel spray width, became larger, whereas for increasing ambient pressure, the fuel film diameter decreased. For most of the investigated ambient pressures, an increase in wall distance led to an increase in film thickness. When the wall distances were small, the film thickness increased with increasing pressure. Furthermore, they stated that the post-impingement spray did not attach to the wall, but slipped radially outwards during the film growing period. Concerning the adhering fuel ratio, the value of this ratio increased linearly with an increase of the wall distance for small wall distances. By increasing the ambient pressure, the adhering fuel ratio was decreased, but the effect of the ambient pressure was found to be small. Only for a large nozzle-to-wall distance, a strong influence of an increase in ambient pressure on the adhering fuel mass was found, where the adhering fuel mass showed a strong decrease. This could be explained by the larger distance between the nozzle and the wall, due to which, at higher ambient pressures, drops could more easily spread into the surrounding gas.

Weiss [186] determined experimentally and theoretically the fraction of the sprayed liquid on the wall for various impingement angles using a flat fan spray directed against a vertical wall with and without additionally supplied wall film. He found that the minima of the deposition fraction were found in the range $40° \leq \alpha_{min} \leq 60°$, where the exact value of the local minimum depended on the ejection pressure of the spray and the presence of the wall film. With an already existing wall film, the spray deposition was lower compared to cases without a wall film. Increasing the ejection pressure led to a reduction of the spray deposition for small impingement angles. For $15° \leq \alpha \leq \alpha_{min}$ Weiss found an increase in deposition for smaller impingement angles, based on the fact that only a minor interaction between the drops of the primary spray and the secondary droplets was expected; hence, the deposition fraction was mainly a result of the single drop impingement dynamics. As the impingement angle was small, this led to a reduction of the number of impinging drops exceeding the critical splashing limit. For $\alpha_{min} \leq \alpha \leq 75°$ an increase in the deposition fraction was found, due to the strong interaction of the impinging drops with the secondary droplets, therefore redirecting the splashed liquid in the direction of the wall.

Pautsch and Shedd [115], Shedd and Pautsch [150] and Pautsch and Shedd [116] performed

an experimental investigation to measure the liquid film thickness and heat exchange created by both a low flow rate single nozzle and a high flow rate four-nozzle array spray design, by making use of a non-intrusive measurement technique based on the total internal reflection. They observed that for some regions, the heat exchange performed better due to the patterns of the flow from the nozzles and the resulting behaviour of the thin liquid surface film. The heat transfer was found to be high where the drops impinged the surface with a high velocity and frequency, maintaining a thin, well-mixed film. As the fluid moved away from the center, a thicker film and larger ripples were observed. For the multiple-nozzle design, flow interactions from neighbouring nozzles were observed, leading to a maximum film thickness in the middle between four neighbouring nozzles, as well as thicker areas along the lines of horizontal and vertical symmetry. At the position of the maximum film thickness, this led to the worst heat exchange. For the single nozzle studies they observed that the drop flux distribution in the spray correlated well with the heat transfer data: a peak of heat transfer was found in the center and lower performances at the corners of the impingement region. These observations could be explained by the fact that at the edges of the spray impingement region the film was much thinner than in the film flow region. For the edges the film thickness was found to be constant and no continuous addition of fresh, cooler liquid was taking place, resulting in less mixing of the film. However, for the center of the impingement region, a continuous stream of impinging drops, perturbing the free surface of the film, was observed, resulting in a good heat exchange.

2.3.2   Modeling film dynamics for spray impingement

Predicting the liquid surface film and the mass distribution in the deposited film is very important in spray impingement applications, since it provides information about the extent of wetting or the heat transfer during cooling. In general, two methods exist for simulating the film dynamics. The first method applies the conservation laws for mass, momentum and energy, by making use of a control volume balance (Stanton and Rutland [161]), or integrates the conservation equations along the coordinate normal to the surface, after which a finite volume method is being used to solve these equations (Bai and Gosman [5]). The second approach uses a particle-based formulation, by tracking the film using Lagrangian numerical particles (O'Rourke and Amsden [109] and O'Rourke and Amsden [111]). The particle tracking method can be applied to relatively coarse grids, without losing its accuracy. In some of these studies, the authors assumed that the film inertia was negligible, but it was shown by Bai and Gosman [5] that this assumption was only valid under special conditions, meaning that the unsteady and convective terms should in general be included in the models for the liquid film.

O'Rourke and Amsden [109], [110] and [111] proposed the most complete film particle tracking method and developed new wall-function models for the transport of vapour mass, momentum and energy in the turbulent boundary layers above the film for their KIVA-3V code. Trujillo *et al.* [172] observed that by neglecting the inertial term of the will momentum equation in the work of O'Rourke and Amsden [110] the film away from the impingement site was significantly underspreaded. In an improved version of their models O'Rourke and Amsden [111] implemented this inertial term and a supplementary pressure term due to impingement. Han *et al.* [55] designed a new submodel for the splash breakup using linear analysis based on the wave phenomena observed on the surface of the liquid crown formed during drop impingement. They stated that the size of the secondary droplets was a function of the Weber and Reynolds numbers of the impinging drops, as well as of the ratio of the liquid density and the ambient gas density. Their new model was implemented in the KIVA-3V code and the results were com-

pared with the new model of O'Rourke and Amsden [111] for the experimental data of a spray impinging on a flat plate under different impingement angles. For the normal impingement, both the experiments and the computations showed that the post-impingement spray formed a symmetrical circular structure and that the computations were close to the experimental results. As the impingement angle decreased, the outer boundary of the spray became elliptical, with a larger radius in front of the impingement location. Here, in general, the computations agreed fairly well with the experiments, but they somewhat overpredicted the normal spray penetration.

Spray impingement source terms for the mass, momentum and energy are usually directly implemented into the governing equations (Bai and Gosman [5], Stanton and Rutland [161], O'Rourke and Amsden [109], [110] and [111]). However, by applying these source terms in this way, some crucial assumptions are made, like very small film surface disturbances, or the neglect of surface tension. These assumptions are not valid at the impingement areas. Trujillo and Lee [174] therefore divided the impingement into two regions: the impingement site, and the region excluding drop impingement. In the latter region, they based their model on a reduced form of the momentum equation, which led to an unsteady-convective equation with wall fraction. Surface tension and gas shear were neglected in this region, as the velocity of the gas flow in this region was small and the disturbances in the film were assumed not to be very significant, and the film velocity was assumed to be sufficiently large. For the impingement region, their model was based on the energy conservation of the drop impingements and on experimental correlations. They implemented their code into the KIVA-3V code and compared their numerical results with the experiments for the film edge displacement and film thickness at different impingement angles. Overall good agreement was obtained for the impingement at angles of 30° and 45°. For the case of 60° impingement, the film front displacement and the film thickness were slightly overpredicted, which was explained by an overprediction of the amount of mass deposited on the wall. They also found that for shallower impingement angles, the film thickness profile became steeper, as more mass was transported from the impingement region to the film edge due to the higher momentum component in forward direction of the impinging drops.

Nagaoka *et al.* [104] used a particle film model in 3D calculations of spark ignition engines, but their model could not predict the transient behaviour of the wall films effectively, because of its assumption that the wall film did not move. Lee and Ryou [79] proposed a new methodology for the spray impingement model, by including several mathematical formulae, based on the energy conservation law and experimental results. Their model for wall films was derived from the research of Nagaoka *et al.* [104], but was modified to be capable of considering the transient behaviour of the wall film deposited on the wall, by solving the continuity and momentum equations for film flows using the integral method proposed by Siwon and Ennaoui [157]. They divided the film formation process into two steps: the initial film formation due to interactions between gravity and surface tension, resulting in a circular disc shape of the deposited drop on the wall, and the transient behaviour of the film moving in radial direction due to the film velocity. They compared their model with the models of Watkins and Wang [184] and of Park [113] for the experiments of Katsura *et al.* [70] for the spray radius and height evolution right after injection. For their model good agreement with the experiments was found, whereas the models of Watkins and Wang and of Park considerably underpredicted the spray height and radius. They indicated that this underprediction resulted from the fact that the splash effect was not included in these models, because they were based on the impingement data onto a hot wall by Wachters and Westerling [180]. Furthermore, Lee and Ryou showed the results of

the simulations for the spray radius, spray height, film radius and average film thickness of the experiments by Saito *et al.* [142]. For the first two characteristics (spray radius and height), a very good agreement between the numerical results and the experiments was found, whereas the averaged film thickness was slightly overpredicted.

The oscillations of the liquid film during spray impingement were also considered in the works of Roisman and Tropea [135] and [138]. In these works, the spray was described as a continuum media, exhibiting specific properties, such as number concentration of particles and their probability density function. The equations of motion of the film on the wall accounted, among others, for the momentum of the fluctuating part of the velocity of the liquid in this film, the volume flux into the film and the pressure produced by the impinging spray. The theory explained the emergence of liquid jets during the impingement of a very intense spray by fluctuations of the pressure (Blondel *et al.* [13] and Wenzel [187], Figure 4). The short times were considered during which the pressure produced by the impinging spray could no longer be considered as continuous over the wall surface. Moreover, the characteristic time and length of these fluctuations were determined.

2.4 Multicomponent planar particle velocimetry measurement techniques

The recent development in experimental measurement techniques has the aim to propose tools for the whole-field investigation of three-dimensional unsteady flows, as well as the complete topology of unsteady coherent flow structures. One good example is flow turbulence, which is three-dimensional, and its full description requires measurement techniques, that are able to capture the instantaneous three-dimensional structure, the vorticity as well as the complete stress tensor. Single probe techniques like *laser-Doppler anemometry* (LDA) and *hot wire anemometry* (HTA), that measure the flow in one point, do not manage to overcome these flow problems. In the last decades, due to faster computers and better image processing and post-processing software, the more-dimensional methods like the *particle tracking velocimetry technique* (PTV) and the *particle image velocimetry technique* (PIV) have become far more relevant in the experimental flow studies.

Both classical two-dimensional PTV and PIV use a laser light sheet to illuminate the flow, hereby following the tracer particles introduced into the flow and imaging the light scattered by the particles, using a multi-exposure imaging technique. In this way, from the displacement of the particles between two subsequent recordings, instantaneous images of the velocity field within the light sheet can be obtained. The difference between the two techniques is the particle density within an image and the way the velocity is determined afterwards. For PIV the particle density in the studied flow is high and for the image processing a group of particle images between two exposures on the same image (*auto-correlation processing*) or on two successive images (*cross-correlation technique*) is being used. For PTV, however, the accurate position and spatial tracking over one, two or more recordings of single particles in the flow is applied, therefore a relatively low particle density is required. The latter technique can often be found in turbomachinery studies, where high pressures and high velocity gradients occur, or in flows where the investigated flow structures are in the order of the correlation window sizes. One of the advantages of PTV is, that individual velocity vectors are calculated with a high accuracy at every point in the flow where a tracer particle is present, thereby solving small scale velocity variations and determining velocity derivatives. A disadvantage of the low seeding density, however, is that the velocity field needs to be interpolated in the post-processing step

to obtain a complete two-dimensional velocity field, which can lead to subsequent errors (Udrea *et al.* [175]). The main problem of the 2D-PTV and 2D-PIV technique is that it only gives information of the flow in a single, stationary slice in the flow. The need for three-dimensional flow information in for example highly turbulent or unsteady flows, and the errors induced by the third velocity component for planar measurement techniques, has led to the extend of the planar measurement techniques to the third spatial dimension. So far, several techniques have been developed, which can be divided into two main classes: those who calculate the three components of the velocity in a two-dimensional domain (*stereo-PIV*, *scanning-PIV*, *dual-plane stereo-PIV*), and those who determine the three-dimensional velocity inside a three-dimensional domain (*3D-PTV*, *holographic PIV*, *tomographic PIV*, *Defocusing digital PIV*, *wavefront sensing technique*, *optical aberrations*).

The most widespread technique for obtaining the third dimension of the studied flow is *stereoscopic imaging* (Gauthier and Riethmuller [48], Prasad and Adrian [119], Westerweel and Nieuwstadt [188], Willert and Gharib [192]). In a stereoscopic camera system the motion of the tracer particles is viewed from two different directions, where the out-of-plane motion of the particles results in slightly different distances travelled by the tracer particles seen from both cameras. By calculating the differences in the apparent in-plane motion, all three components of the tracer displacements can be determined. In turbulent boundary layer flows, where the velocity fluctuations can be very small, a high level of measurement accuracy is required, to determine the small differences in displacement seen by the two cameras.

Two categories are usually distinguished for stereoscopic PIV, having different optical properties: the translation method and the angular displacement method. In the translation method, the optical axes of the imaging lenses are parallel to the normal of the object plane (Gauthier and Riethmuller [48]). By placing the image planes parallel to the object planes, the image magnification is independent of the position in the image and object planes. When the image sensors are placed at a small off-axis distance, this leads to a complete overlap of the fields of view of both cameras (Prasad and Adrian [119]). This method is characterised by its convenient mapping and well-focused images over the whole observation area. However, the off-axis distance increases in proportion to the stereoscopic viewing angle. The major drawback of this technique is that when this angle becomes too large, this results in a non-paraxial imaging of the objects, leading to a deterioration of the image quality as a result of the optical aberrations. Westerweel and Van Oord [190] showed that for an image magnification of $M = 0.3$, the minimum stereoscopic viewing angle allowed to avoid optical aberrations was about 15°. The same angle was found in the investigation of the velocity field on a well-established isotropic grid generated turbulent flow (Lecerf and Trinité [75]). They observed, that for an off-axis angle of 15° an error less than 0.5% of the on-axis measured displacement was found.

In case the angular method is used, the optical axes of the imaging lenses are both at an angle θ with respect to the normal of the object plane. In this way, for any value of the stereoscopic viewing angle, the imaging remains paraxial. When the CCD sensors of the cameras are placed perpendicular to the optical axis, this results in particle images away from the optical axis that are out-of-focus. Normally, this is compensated by applying the so-called *Scheimpflug condition*, where the sensor is tilted with respect to the lens plane, so that each part of the image is in focus. This tilting angle depends on the image magnification, M, and the angle between the optical axis and the normal of the object plane. Gauthier and Riethmuller [48] showed that the best accuracy of the third velocity component was obtained for an angle of 45° between the optical axis and the normal of the object plane. One major drawback of this technique is that the magnification is no longer constant in the complete image plane. This

leads to an extra step in the image processing part, the so-called back-projection procedure, which is discussed in detail by Westerweel and Van Oort [190]. Furthermore, due to the spatial separation of the two cameras, a large optical window is required. Another problem of the angular method is that the fields of view of both cameras are not identical. By placing the cameras at an optimised position, an overlap of the two fields of view of 94% can be reached.

Since its introduction in 1998 (Santiago *et al.* [145]) micron resolution particle image velocimetry (*Micro-PIV*) has become established as an experimental tool for the measurement of velocity profiles in microfluidic devices. Micro-PIV measurements are usually restricted to the components of the velocity within the plane of the Micro-PIV images, thus analysing the two-dimensional flow. Bown *et al.* [16] and Lindken *et al.* [86] developed a stereoscopic micro-PIV system for the simultaneous measurement of all three velocity components in a measurement plane in a closed microchannel. By using a large diameter stereo objective lens in combination with two off-axis beam paths, stereoscopic viewing was achieved. With the use of two CCD cameras, the stereo-PIV images were captured. As a calibration by means of a calibration target was not possible due to the small working area under the microscope, a calibration based on the self-calibration of the tracer particle images was required (Wieneke [191] and Lindken *et al.* [86]). A drawback of this technique is that a stereo-objective with a low numerical aperture and a large depth-of-focus is required.

Another way of extending the two-dimensional PIV to quasi-three-dimensional volumetric measurements is by using the *scanning-PIV technique*. This technique is directly derived from the standard two-dimensional PIV or stereo-PIV by making use of a scanning laser light sheet through the measurement volume (Brücker [19]). The scanning light sheet continuously samples the flow in depth in successive planes, where the particle image patterns are recorded. The subsequent recording at a certain plane inside the measurement volume can either be taken directly after the last recording, or after the complete scan of the volume. In this way, planar velocity fields are obtained, slightly shifted in time and space from one another, which can afterwards be combined to return three-dimensional velocity fields. Brücker [19] used the scanning-PIV technique in combination with one video camera to study the three-dimensional temporal vortical structures in a cylinder wake. The out-of-plane component of the velocity was evaluated by integrating the continuity equation. This method, however, could only be used when the third velocity component of the studies flow was known at the boundary of the integration domain. He therefore presented a year later the scanning stereo-PIV technique, based on a combination of the stereo-PIV technique and the quasi-three-dimensional scanning-PIV technique (Brücker [20]). For this technique, he used two cameras with a frame rate of 25 Hz in combination with a scanning laser light sheet to study the wake flow behind a spherical cap at $Re = 100$. However, since the frame rate of the cameras was low, this technique was limited to only 9 slices, due to which the finer scale of the eddies at higher Reynolds numbers could not be solved. This study showed, that high-repetition camera systems (kHz) are required to assure that the complete scanned volume is recorded at almost the same time. Hori and Sakakibara [61] measured a turbulent jet in water at low Reynolds numbers of $Re \approx 1000$, where 50 measurement slices in the volume were captured within 0.22 s. The drawbacks of this technique, however, are the high costs for high repetition rate lasers and the relatively low laser beam intensity, as well as the more complicated set-up compared to stereo-PIV. Shinohara *et al.* [154] and Angele *et al.* [3] developed a high-speed scanning Micro-PIV system to study the time resolved, pseudo-three-dimensional flow field in micro fluidics. Two different methods were studied to obtain the third dimension of the velocity vectors. Angele *et al.* [3] used a rotating disc having ten glass windows with different thicknesses. The disc rotated at 6000 *rpm*, corresponding to a

scanning frequency of 100 Hz. As every glass plate had a different thickness, the optical lengths underneath the objective lens were varied, resulting in a rapid movement of the focal plane of the micro-PIV system in the out-of-focus direction. In this way, a depth resolution of 5 μm was achieved when measuring in water. Shinohara *et al.* [154] obtained the three-dimensional velocity field by using an objective lens equipped with a piezo-actuator. The amplitude and frequency of the displacement were determined by the voltage and frequency of the input signal.

Kähler and Kompenhans [67] introduced an alternative to scanning PIV, the so-called *dual-plane stereo-PIV*, where the particle images in different planes were recorded simultaneously by using different laser wavelengths or light polarization to distinguish the scattered light from the two planes. Separation by laser light polarisation is the most commonly adopted solution of the two possible techniques; however, only two imaging planes can be used in this way. Measurements can also be performed over more than two planes in the measurement volume, but in this case each plane requires its own double-pulse laser source, which makes this alternative significantly more expensive. Furthermore, by using different colors the optical arrangement is being made significantly more complicated. Veerman and Den Boer [177] investigated an alternative to the dual stereo-PIV technique, where both laser light sheets were misaligned to a certain amount, in this way introducing an "upstream" light sheet and a "downstream" light sheet to compensate for the out-of-plane displacement and have the same particles illuminated by both laser pulses. In case one camera was used, this arrangement could only be used for flows with a constant out-of-plane component, due to the limited depth of field of the optics. This problem was solved by using two digital cameras, one focussed upstream, the other one downstream. They tested their arrangement on a swirling nozzle flow, having an out-of-plane component up to a factor 3 larger than the largest in plane component, and found that the results showed a relatively large amount of unmatched particles between the two laser sheets, due the out-of-plane displacements which caused the signal-to-noise ratio to deteriorate.

Three-dimensional particle tracking velocimetry (3D-PTV) or *three-dimensional particle streak velocimetry* are PIV techniques, based on a volume illumination, where multiple camera systems are used to track individual particles in space as they move along with the studied flow. This results in a Lagrangian representation of the flow (Chiu and Rib [22], Nedderman [105], Racca and Dewey [123]). The exact position of a particle within the volume is given by the intersection of the lines of sight corresponding to a particle image in the recordings from all viewing directions. The advantages of this three-dimensional measurement technique in comparison to the aforementioned ones are the absence of moving parts and the fully digital and fully three-dimensional character. The velocity determination in the measurement volume is reached by either particle tracking or by three-dimensional cross-correlation with artificially created particles (Schimpf *et al.* [152]). As was mentioned before, one of the major disadvantages of the particle tracking technique is the required low seeding density, to avoid a complicated particle identification in the images and a high probability of particle image overlapping. Due to this relatively low seeding density, the resolution of the velocity spatial distribution is also found to be lower than for digital PIV, therefore many recordings are needed for a good three-dimensional representation of the studies flow. Another drawback of this technique is that the lines of sight of the different cameras for a particle almost never truly intersect, as a result of which an intersection criterion is needed. Details on the experimental implementation of the method as well as on the accuracy of the method can be found in Virant and Dracos [178], Virant [179], Sinha and Kuhlman [155] and Racca and Dewey [123].

One of the three-dimensional velocimetry techniques, which has received the most attention in the last decades, is *holography-PIV* (Barnhart *et al.* [9], Sheng *et al.* [151], Tao *et al.* [164], Zhang *et al.* [199], Hinsch [58], Garcia-Sucerquia *et al.* [47]). Digital in-line holography, in which a single laser beam is used, is the most used arrangement. The laser beam travels through a particle cloud and is directly recorded onto a CCD chip of the camera, without using an optical system (Malkiel *et al.* [90]). However, due to difficulties in generating a small depth of focus, low particle densities for in-line holographic recordings are required, resulting in the fact that this technique does not allow a detailed PIV correlation analysis, but is mostly used in combination with PTV. To measure the three-dimensional instantaneous velocity distribution over a finite volume at a resolution of millions of vectors, an off-axis recording of a laser sheet is necessary. Meinhart *et al.* [94] showed that with holographic PIV the measurement of about 10^5 instantaneous velocity vectors in a flow volume of $100 \times 100 \times 100$ mm^3 was achievable. This technique is based on the interference pattern of a reference light beam with scattered laser light by the particles. These interference patterns are recorded on a hologram, after which the particle location in depth is determined. The position of the diffraction pattern in the image gives the in-plane position of the particle. The original light intensity field in the measurement volume at the time of recoding can be reproduced by illumination of the hologram with the reference light. In these reproduced images, the intensity is the highest at the original tracer particle position. By subsequent scanning of the reconstructed intensity fields, digital intensity maps are made, which can be analysed by applying the processing techniques such as PIV or PTV, in order to get the velocity fields.

For measuring the third component of the velocity field three possibilities are available: stereoscopic holography, using the focussing difference between two images and multiple light sheet holography. The first method is based on the stereoscopic effect, introduced by observing the particles through two different regions of the hologram, or through two different holograms. Fabry and Sieverding [41] applied this technique to investigate the flow in a turbomachine to study the swirling flow. They were, however, not capable of measuring the reverse wake flow, as they used an auto-correlation technique for their analysis. As holography provides a three-dimensional position for each particle, the third component can also be analysed directly from the focussing difference between the two image pairs. Royer [140] and Monnier [99] showed that for this latter technique, the accuracy of the third velocity component was not good due to the fact that the evolution in depth of the particle images is blurred by the holographic noise. Hinsch [57] used four parallel light sheets in which the flow was double-exposed and recorded on holographic plates. This technique provided the instantaneous flow simultaneously in several planes in the volume, but was limited to only a few light sheets separated in space from one another. The major drawbacks of holographic PIV are the requirement of digital cameras with high data storage possibilities, as well as the complicated and time consuming evaluation processes.

A relatively new measurement technique to determine the three dimensional three component velocity inside a volume is *tomographic 3D-PIV*. This measurement technique has been described in detail by Elsinga *et al.* [33], [36] and [35], therefore only a small overview of the working principle of Tomo-PIV will be given here. Tracer particles within the measurement volume are illuminated by a pulsed light source. The scattered light pattern is recorded simultaneously from several viewing directions using CCD cameras in a similar arrangement as for stereo-PIV. By making use of the *Scheimpflug condition* in two directions between the image plane, the lens plane and the mid-object-plane, the entire volume is in focus. From its projections on the CCD arrays, the three-dimensional particle distribution is reconstructed

as a three-dimensional light intensity distribution. This reconstructed three-dimensional particle distribution is not unique; therefore the most delicate part of this measurement technique is to determine the most likely three-dimensional distribution. By making use of the three-dimensional cross-correlation between the reconstructed particle distributions for both exposures, the three-dimensional tracer particle displacement field is obtained. A calibration procedure, similar to the one used in stereo-PIV and 3D-PTV, is required to obtain a relation between the image coordinates and the physical space. Each camera records the calibration target at different positions in the volume, after which for each camera these images are used to determine the viewing direction and the field of view. They applied the Tomo-PIV technique to different aerodynamical studies, like the three-dimensional instantaneous velocity and vorticity fields within a circular cylinder wake and the three-dimensional vortex structure within a turbulent boundary layer. This technique has the advantage of being able to record the instantaneous three-dimensional velocity field, independent of the flow speed. The accuracy of this technique is given by the particle seeding density and the number of cameras used. However, to successfully reconstruct the particle images, the accuracy of the calibration has to be very good (typically in the order of 0.4 pixels, Elsinga *et al.* [34]). Furthermore, a good optical access to the measurement volume is required, as multiple cameras are being used.

Soria and Atkinson [159] introduced a new method that used multiple digital CCD cameras to record in-line digital holograms of the same measurement volume from multiple orientations. Their arrangement used the same basic equipment as Tomo-PIV, but the camera lenses were taken off, in order to overcome the depth of field problems associated with digital in-line holography and to avoid the complex optical calibration of Tomo-PIV. This resulted in a three-dimensional reconstruction of the tracer particles within the measurement volume, which could then be analysed using normal three-dimensional cross-correlation algorithms to obtain the three-dimensional velocity field. In contrast to Tomo-PIV, this technique has the advantage of directly providing the three-dimensional intensity fields, canceling one of the major sources of possible experimental errors of Tomo-PIV.

Another relatively new approach to the three-dimensional visualisation of flow fields is *defocusing digital PIV, DDPIV*, introduced the first time by Willert and Gharib [193]. DDPIV has one unique optical axis and is based on pattern matching, rather than on stereoscopic matching of particle images. The main feature of DDPIV is the quantitative use of blurring of illuminated particles displaced from the reference plane, where the particle images would appear in focus. The arrangement consists of a single lens in combination with a mask with two or more apertures, shifted away from the optical axis, to obtain multiple images of the particles. Two different approaches are found in literature for the mask used for DDPIV: three apertures arranged in a triangle (Willert and Gharib [193]) and an angular aperture (Lin *et al.* [84]).

For most applications, the mask consists of three small apertures, placed in a triangular way around the center of the mask. In this way, each particle will be imaged as three points, arranged in an equilateral triangle. The shift between these multiple images is a direct measure for the depth location of the tracer particle. The algorithms for analysing the three-dimensional position of the particles has been explained in detail in the literature (Willert and Gharib [193], Pereira *et al.* [117], Pereira and Gharib [118], Gharib *et al.* [50]). With a two-aperture mask, there would exist a depth ambiguity, as there exist two positions, front and back of the reference plane, where a particle forms exactly the same image pair. To overcome this non-uniqueness problem, a mask with three apertures was used, due to which the orientation of the triangle indicated the relative position of the particle with respect to the reference plane. By using only

one camera, the problem of image overcrowding can appear. To overcome this problem, Pereira *et al.* [117] changed their optical arrangement from using one single camera to applying three cameras, where behind each aperture a single camera was placed. In this way higher particle densities could be used and an arbitrary aperture spacing was allowed. The drawback of this technique is the small diameter of the apertures, due to which just a fraction of the total laser light intensity reaches the camera. Therfore, a high laser power is required in combination with larger tracer particles.

In the second approach, where an annular aperture is used, a ring-shaped image is observed on the CCD camera when the tracer particle is out-of-focus. From the diameter of this defocused particle image, which is a function of the outer and inner diameter of the ring-aperture, the depth position of the tracer particle can be determined. There exists, however, a depth non-uniqueness problem, as the same particle image can be formed at two positions from the mask. This could be overcome by changing the shape of the angular aperture above the middle line with respect to the shape below, or visa-versa. In comparison to the first approach, where a triangular aperture is used, this second approach can resolve overlapping particle images, which appear on the image as interlocking rings, and therefore a higher particle density is possible. Furthermore, as the aperture is larger, a higher amount of the laser light intensity reaches the CCD chip. This makes this arrangement also suitable for microscopy.

Towers *et al.* [169] and Angarita-Jaimes *et al.* [2] introduced a relatively new and not well-known three-component, three-dimensional measurement technique, that uses a single camera, the so-called *wavefront sensing*. This method is based upon the measured wavefront scattered by the tracer particles, from which afterwards the position of the tracer particles in space can be determined. They described two approaches to capture the data required to measure the wavefront: multi-planar imaging using a distorted diffraction grating together with a phase diversity analysis, and an anamorphic technique. With the first technique, three images are obtained per tracer particle, corresponding to the three diffraction orders. The image diameters are linearly related to the distance of the particle from the focal plane. In this way the three-dimensional position of the tracer particles can be determined. It was shown, that with this method, a high resolution for the out-of-plane component of the particle position of about $8\ \mu m$ could be achieved. The anamorphic imaging makes use of a combination of a cylindrical lens with a spherical lens, producing for each particle a different image size in the horizontal and vertical direction. Each tracer particle image is analysed, hereby defining the length of the major and minor axis of each particle (the different data processing steps will be discussed in detail in Chapter 8). These two lengths are a direct measure of the particle position in depth. The accuracy in depth of the second technique depends strongly on the resolution of the CCD chip of the camera. Angarita-Jaimes *et al.* [2] received an average depth resolution of $36\ \mu m$. The advantage of this technique, is that it produces a single image on the CCD chip for each tracer particle, and is therefore more suitable for flows with a high particle density.

The last three-dimensional, three-component volume measurement technique is still under development, and was first introduced by Hain and Kähler [53]. This technique also requires only one camera to investigate the three-dimensional velocity, as the depth position of the tracer particles is encoded by the use of an optical aberration called astigmatism. In their experiments, astigmatism was introduced by aligning a single camera, mounted on a *Scheimpflug adapeter*, to the measurement volume at a certain angle. This angle, in combination with the refraction indices of the different materials through which the scattered light by the particles passed, resulted in astigmatism. Due to the introduced astigmatism, the particle images had